

3 - OCT 1958  
15485

Copy 255  
RM L58F24

NACA RM L58F24

7845

~~CONFIDENTIAL~~



0144753

TECH LIBRARY KAFB, NM

# RESEARCH MEMORANDUM

ANALYSIS OF PRESSURE DATA OBTAINED AT TRANSONIC SPEEDS  
ON A THIN LOW-ASPECT-RATIO CAMBERED  
DELTA WING-BODY COMBINATION

By John P. Mugler, Jr.

Langley Aeronautical Laboratory  
Langley Field, Va.

~~CLASSIFIED DOCUMENT~~

~~Information affecting the national defense of the United States within the meaning of Executive Order 12958, Section 1.5, is hereby designated as information the disclosure of which in any manner to an unauthorized person is prohibited by law.~~

NATIONAL ADVISORY COMMITTEE  
FOR AERONAUTICS

WASHINGTON

September 26, 1958

~~CONFIDENTIAL~~

~~CONFIDENTIAL~~

Classification cancelled (or changed to UNCLASSIFIED)

By NSA TECH PUB ANNOUNCEMENT #39  
(OFFICER AUTHORIZED TO CHANGE)

By 16 FEB 61  
NAME AND

ALB  
GRADE OF OFFICER MAKING CHANGE)

17 MAR 61  
DATE



## NATIONAL ADVISORY COMMITTEE FOR AERONAUTICS

## RESEARCH MEMORANDUM

## ANALYSIS OF PRESSURE DATA OBTAINED AT TRANSONIC SPEEDS

## ON A THIN LOW-ASPECT-RATIO CAMBERED

## DELTA WING-BODY COMBINATION\* \*\*

By John P. Mugler, Jr.

## SUMMARY

An investigation has been made in the Langley 8-foot transonic tunnels to determine the aerodynamic loading characteristics of a thin conical cambered low-aspect-ratio delta wing in combination with a basic Sears-Haack body and a body indented symmetrically for a Mach number of 1.2. The wing had an aspect ratio of 2.31 and had NACA 65A003 airfoil sections parallel to the model plane of symmetry over the uncambered portion. The tests were conducted at Mach numbers from 0.60 to 1.12 and at 1.43 and at angles of attack from  $-4^\circ$  to  $20^\circ$ .

The results indicate that a leading-edge separation vortex causes the shape of the spanwise load distributions to change at moderate angles of attack. Rearward and outboard center-of-pressure movements of the order of 9 percent of the mean aerodynamic chord and 2 percent of the semispan, respectively, are noted at transonic speeds. Body indentation had little effect on the aerodynamic loading characteristics. Comparisons with experimental data for a similar plane wing indicate that the cambered wing is considerably more effective in developing leading-edge thrust.

## INTRODUCTION

Wind-tunnel and flight tests have shown that conical leading-edge camber on a thin low-aspect-ratio delta wing results in increasing the

\*The information presented herein was offered as a thesis in partial fulfillment of the requirements for the degree of Master of Science in Aeronautical Engineering, Virginia Polytechnic Institute, Blacksburg, Virginia, May 1958.

\*\*Title, Unclassified.

~~CONFIDENTIAL~~

lift-drag ratio at transonic and low supersonic speeds (refs. 1 and 2). Therefore, a wing of this description has been included in a general program being conducted in the Langley 8-foot transonic tunnels to investigate the detailed pressure distributions and loads on a series of thin wings suitable for transonic and supersonic flight. References 3 and 4 present the results of two previous investigations of this general program. Detailed pressure distributions at transonic and low supersonic speeds on a thin conical cambered low-aspect-ratio delta wing in combination with basic and indented bodies have been presented in reference 5. A more detailed analysis of the pressure distributions of reference 5 is presented herein in terms of total section loads and overall wing-body characteristics.

## SYMBOLS

$b$  wing span to rounded tips

$c$  airfoil section chord, measured parallel to plane of symmetry

$\bar{c}$  wing mean aerodynamic chord

$c_{av}$  average wing chord

$c_{m,c/4}$  wing section pitching-moment coefficient about  $0.25c$ ,

$$\int_0^1 (C_{p,L} - C_{p,U}) \left(0.25 - \frac{x}{c}\right) d\left(\frac{x}{c}\right)$$

$C_{m,w}$  wing pitching-moment coefficient about  $0.25\bar{c}$ ,

$$\int_{\frac{r}{b/2}}^1 c_{m,\bar{c}/4} \frac{c^2}{c_{av}\bar{c}} d\left(\frac{y}{b/2}\right)$$

$c_{m,\bar{c}/4}$  wing section pitching-moment coefficient about  $0.25\bar{c}$ ,

$$c_{m,c/4} + c_n \left( \frac{x_{\bar{c}/4}}{c} - \frac{x_{c/4}}{c} \right)$$

$C_{m,fw}$  body pitching-moment coefficient about  $0.25\bar{c}$ , based on wing area and  $\bar{c}$ ,

$$\frac{2\pi l^2 D_{max}}{S\bar{c}} \int_0^{1/4} \int_0^1 \cos \theta \frac{r}{r_{max}} (C_{p,L} - C_{p,U}) \frac{x_{c/4} - x}{l} d\left(\frac{x}{l}\right) d\left(\frac{\theta}{2\pi}\right)$$

- $C_m$  total pitching-moment coefficient,  $C_{m,w} + C_{m,fw}$
- $c_n$  wing section normal-force coefficient,  $\int_0^1 (C_{p,L} - C_{p,U}) d\left(\frac{x}{c}\right)$
- $C_{N,w}$  wing normal-force coefficient,  $\int_{\frac{\bar{r}}{b/2}}^1 c_n \frac{c}{c_{av}} d\left(\frac{y}{b/2}\right)$
- $C_{N,fw}$  body normal-force coefficient based on wing area,  

$$\frac{2l\pi D_{max}}{S} \int_0^{1/4} \int_0^1 \cos \theta \frac{r}{r_{max}} (C_{p,L} - C_{p,U}) d\left(\frac{x}{l}\right) d\left(\frac{\theta}{2\pi}\right)$$
- $C_N$  total normal-force coefficient,  $C_{N,w} + C_{N,fw}$
- $C_{B,w}$  wing bending-moment coefficient about wing-body center line,  

$$\int_{\frac{\bar{r}}{b/2}}^1 c_n \frac{c}{c_{av}} \left(\frac{y}{b/2}\right) d\left(\frac{y}{b/2}\right)$$
- $C_p$  pressure coefficient,  $\frac{p - p_\infty}{q_\infty}$
- $D_{max}$  maximum body diameter
- $l$  body length
- $L$  body length for complete closure at base
- $M$  Mach number
- $p$  local static pressure
- $p_\infty$  free-stream static pressure
- $q_\infty$  free-stream dynamic pressure
- $\bar{r}$  root-mean-square body radius between wing-body leading-edge and trailing-edge junctures

$r_{\max}$	maximum body radius
$r$	body radius at any station
$S$	wing area
$x$	distance from leading edge of wing or nose of body (positive rearward)
$\frac{x_{cp}}{\bar{c}}$	wing chordwise center of pressure measured from leading edge of $\bar{c}$
$y$	spanwise distance measured from body center line
$\frac{y_{cp}}{b/2}$	wing spanwise center of pressure measured from wing-body center line
$z$	vertical distance from wing chord line of uncambered section
$\alpha$	angle of attack of wing-body center line
$\theta$	meridian angle of body orifice station ( $\theta = 0^\circ$ at station A)

Subscripts:

$le$	leading edge
$L$	lower surface
$U$	upper surface
$e$	exposed

APPARATUS

Tunnels

The investigation at subsonic and transonic speeds was conducted in the Langley 8-foot transonic tunnel. This facility is a single-return wind tunnel operated at approximately atmospheric stagnation pressures. The dodecagonal-shaped test section has been slotted longitudinally to allow testing through sonic speeds with negligible effects of choking and blockage. A description of the tunnel and its calibration is given in reference 6. Data at a Mach number of 1.43 were obtained in the Langley 8-foot transonic pressure tunnel by enclosing the longitudinal

slots with specially designed channels which converted the slotted test section to a supersonic nozzle. Details of the resulting nozzle shape and the test-section Mach number distribution are given in reference 7.

### Models

The delta wing tested has  $60^\circ$  sweepback of the leading edge, a taper ratio of 0, and NACA 65A003 airfoil sections parallel to the model plane of symmetry over the uncambered portion of the wing. Model details are shown in figure 1(a). The leading-edge portion of the wing has conical camber over the outboard 15 percent of each semispan. The amount of leading-edge vertical displacement at any spanwise station (denoted  $z_{le}$  fig. 1(b)) was obtained from reference 8 for a lift coefficient of 0.15 near  $M = 1.0$ . Then a parabolic mean camber line  $\left( z = z_{le} \left( 10.7181 \frac{x^2}{y^2} - 6.5466 \frac{x}{y} + 1 \right) \right)$  was fitted in the streamwise direction between the displaced leading edge and a line at 85 percent of the local semispan. Next, the thickness distribution of the plane wing was sheared vertically until it was distributed evenly about the parabolic mean line. Details of the camber distribution and ordinates for the cambered sections are presented in figure 1(b). The actual wing plan form deviated from the theoretical delta wing plan form in that the wing tips were rounded. Rounding the tips reduced the wing area by a small amount (a reduction of 0.6 percent of the total wing area of 0.855 square foot) and produced negligible changes in mean-aerodynamic-chord length and location. The theoretical aspect ratio, which assumes pointed tips, is 2.31, and the actual aspect ratio based on the rounded tips is 2.06. The wing was constructed of steel and was tested as a midwing configuration.

The wing was tested in combination with basic and indented bodies. The basic body is a body of revolution designed to have minimum wave drag for a given length and volume. This body is a Sears-Haack body and its shape can be expressed by the equation for the radius of the body as

$$r = r_{\max} \left[ 1 - \left( 1 - \frac{2x}{L} \right)^2 \right]^{3/2}$$

In this equation  $L$  represents the length of the body for complete closure at the rear end. For this body  $L = 40.2$  inches. The necessity for providing a region at the rear end of the body to accommodate the sting support required that the actual body length be less. For this configuration the actual body length was about 90 percent of the length for complete closure.

~~CONFIDENTIAL~~

The other body was a body of revolution indented symmetrically for a Mach number of 1.2 in accordance with the supersonic-area-rule concept of reference 9. Photographs of the basic and indented wing-body combinations are shown in figures 1(c) and 1(d), respectively. Ordinates for both bodies have been presented in reference 5.

### TESTS

Both the basic and the indented wing-body combinations were tested at Mach numbers from 0.60 to 1.12 and at a Mach number of 1.43. Generally, the angle-of-attack range extended from  $-4^{\circ}$  to  $20^{\circ}$ .

Transition strips were fixed on both configurations during all the tests. The strips were about 0.10 inch wide and were formed by sprinkling No. 120 carborundum grains on a plastic adhesive. The strips extended from the wing-body juncture to the wing tip at 10 percent of the local chord on the upper and lower wing surfaces and formed a ring around the body at 10 percent of the body length.

The Reynolds number based on the wing mean aerodynamic chord varied during the tests from about  $2.8 \times 10^6$  at a Mach number of 0.60 to  $3.3 \times 10^6$  at the highest test Mach number of 1.43. The free-stream dynamic pressure varied from about 400 to 900 pounds per square foot over the same Mach number range.

### MEASUREMENTS AND ACCURACY

Measurements of the local static pressures on the models were made by use of orifices distributed over the upper and lower wing surfaces at three wing semispan locations and along five body meridian rows. Orifice locations are given in figure 2. The pressure coefficients determined from these measurements have been published in reference 5 and are estimated to be accurate within  $\pm 0.005$ . The section and total loadings presented herein were obtained by fairing and integrating the pressure-coefficient distributions over the surfaces. In obtaining the total loadings the assumption was made that all three rows of wing orifices were on one panel.

The angle of attack of the model was measured by means of a strain-gage attitude transmitter mounted in the nose of the model and is estimated to be accurate within  $\pm 0.1^{\circ}$ . Calibrations of the Langley 8-foot transonic tunnel with the test section empty indicate that local deviations from the average free-stream Mach number are of the order of  $\pm 0.003$ .



at subsonic speeds. With increases in Mach number, these deviations increased but did not exceed  $\pm 0.010$  at  $M = 1.2$ . (See ref. 6.) In the Langley 8-foot transonic pressure tunnel at  $M = 1.43$ , local deviations from the average free-stream Mach number did not exceed  $\pm 0.015$  in the region of the model during these tests (ref. 7). The average free-stream Mach number was held to within  $\pm 0.003$  of the nominal values shown in the figures.

### CORRECTIONS

No corrections have been applied to any of the data for boundary-interference effects. At subsonic speeds, the slotted test section minimized boundary-interference effects such as blockage and boundary-induced upwash. At  $1.03 < M < 1.12$  boundary-reflected disturbances struck the model; therefore, no data were recorded in this Mach number range.

No corrections have been applied to any of the data for the effects of wing aeroelasticity. In order to provide an indication of the magnitude of these effects, some of the aeroelastic twist characteristics have been calculated and published in reference 5. These calculations show that maximum aeroelastic twist angles of the order of  $-2^\circ$  were encountered at  $M = 1.03$  and  $\alpha = 20^\circ$ .

### RESULTS AND DISCUSSION

The results of this investigation are presented in figures 3 to 11. Since staggered scales have been used on many of the figures, care should be taken in selecting the proper reference axis for each curve. In figure 3(d) at  $M = 1.43$ , note that the data for the indented-body configuration were not obtained at the two highest angles of attack. In figures 6 and 7 note that force data for  $M = 1.43$  are not available for the configurations.

#### Spanwise Load Distributions

The spanwise load distributions were obtained by integration of the chordwise pressure distributions of reference 5 and are presented in figure 3. At  $\alpha = 0^\circ$  the span loadings generally showed a small negative loading over the majority of the span. This negative loading would be expected, however, since with this type of camber the outboard wing sections are operating at a lower angle of attack than the wing-body

center line. As the angle of attack is increased to  $4^\circ$  at  $M = 0.60$  (fig. 3(a)), the spanwise load distribution becomes approximately elliptical in shape. Further increases in angle of attack cause the shape to progressively deviate more and more from elliptical and approach triangular at  $\alpha = 20^\circ$ . Examination of the chordwise pressure distributions in reference 5 has indicated the presence of a leading-edge separation vortex over the wing at moderate to high angles of attack. This vortex causes radical changes in the chordwise pressure distributions at the outboard wing stations (see fig. 5(a) of ref. 5) which result in the changes in shape noted for the spanwise load distributions. As the Mach number is increased above  $M = 1.0$ , the effect of this vortex on the spanwise load distributions is not as prominent as it was at the lower Mach numbers (figs. 3(b) to 3(d)). However, there is indication that it is still present on the wing even at  $M = 1.43$ . At the negative angle of attack of  $-4^\circ$  the shape of the spanwise load distribution is somewhat unusual at all Mach numbers except 1.43. The chordwise pressure distributions of reference 5 indicate that the leading-edge separation vortex has already formed over the wing at this angle of attack and is responsible for the unusual span loading shape.

The wing-body juncture locations for the basic and indented bodies shown in figure 3 were obtained by taking the root-mean-square value of the body radius over the region of the body intersected by the wing. The resulting values were  $0.198b/2$  and  $0.188b/2$  for the basic and indented bodies, respectively.

Also shown in figure 3 is the average body normal-load coefficient for both the basic and indented configurations. This coefficient is defined so that the area under this curve from the wing-body center line to the wing-body juncture is equal to the normal-force coefficient for the body in the presence of the wing. Therefore, it indicates the average magnitude rather than the distribution of the load over the body.

#### Force and Moment Characteristics

Aerodynamic force and moment characteristics for the wing in the presence of the body were obtained by fairing and integrating the spanwise load distributions and are presented in figure 4. Force and moment characteristics for the body in the presence of the wing were obtained similarly and are presented in figure 5. The data of figures 4 and 5 were combined to obtain the aerodynamic characteristics of the wing-body combination and these are presented for the basic and indented configurations in figures 6 and 7, respectively. The data of figures 6 and 7 show that, in general, both the force- and moment-coefficient curves exhibited nonlinearities even at low normal-force coefficients. These nonlinearities result from the formation of the leading-edge separation

vortex on the wing at low angles of attack as noted previously. At the higher normal-force coefficients, an abrupt destabilizing tendency (see figs. 6(b) and 7(b)), which is characteristic of sweptback wings, is apparent at  $M = 0.90$  and  $0.94$ .

Also shown in figures 6 and 7 is a comparison between the force and moment characteristics obtained by integrating the pressure distributions and those obtained on the same configuration from the force tests of reference 2. The agreement between these two sets of data is very encouraging, particularly when it is considered that the pressure wing had chordwise rows of orifices at only three spanwise positions.

#### Center-of-Pressure Characteristics

The longitudinal and lateral center-of-pressure characteristics for the wing were computed by using the data from figure 4 and are presented in figure 8. Center-of-pressure movements were noted at transonic speeds through the range of normal-force coefficients tested (fig. 8(a)). Rearward and outboard movements of the order of 9 percent of the mean aerodynamic chord and 2 percent of the semispan, respectively, occurred rather rapidly between  $M = 0.85$  and  $1.0$ . As the Mach number was increased above  $1.0$  at a constant normal-force coefficient, the center-of-pressure location appeared to begin to stabilize at its supersonic value. The effect of the abrupt destabilizing tendency (noted in figs. 6(b) and 7(b)) on the center-of-pressure location can be seen in figure 8(b). Generally, significant forward and inboard movements are apparent at Mach numbers through  $0.94$ . Of course, the magnitude and abruptness of these movements are consistent with the moment curves of figure 4.

#### Division of Normal Load

The division of normal load has been computed for both the basic and indented configurations and is presented in figure 9. These results indicate that the division of normal load was little affected by Mach number at low normal-force coefficients, the ratio being about  $0.77$  or  $0.78$  through the Mach number range. Increases in normal-force coefficient resulted in a decrease in the fraction of the load carried by the wing at all Mach numbers. The ratio of exposed wing area to total wing area, denoted for the two configurations by the lines labeled  $S_e/S$  in figure 9, gives a poor prediction of the results, as would be expected for a low-aspect-ratio configuration.

### Effects of Body Indentation

Data for the indented body configuration is presented and compared with data for the basic body configuration in figures 3, 4, 5, 8, and 9. Generally, the effects of body indentation are small. Figure 8, which shows a comparison of the center-of-pressure characteristics for the basic and indented body configurations, indicates that body indentation causes a slight delay in the transonic rearward and outboard center-of-pressure movement (fig. 8(a)). In addition, body indentation was responsible for some changes in center-of-pressure location at high normal-force coefficients, particularly at  $M = 0.94$  (fig. 8(b)).

### Comparison With Plane Wing

Pressure measurements on a plane delta wing of the same plan form and airfoil sections as the wing discussed herein are given in reference 10. The body used in reference 10 is not identical to the basic body used for the present investigation; however, the differences are small and will not invalidate the comparisons to be made herein.

As noted in the introduction a considerable performance benefit was realized when the plane wing was conically cambered. Reference 2 shows that at  $M = 0.80$  the maximum lift-drag ratio for the cambered wing is about 22 percent higher than that for the plane wing, and the maximum lift-drag ratio occurs at a lift coefficient of about 0.2. In order to show an example of how the camber effected this increase in lift-drag ratio, a comparison has been made at  $M = 0.80$  and  $\alpha \approx 4^\circ$  ( $c_n \approx 0.2$ ) of the pressure distributions at about midspan ( $\frac{y}{b/2} = 0.53$ ) on the plane and cambered wings. Figure 10 shows the pressure coefficients plotted against thickness in fraction of chord for both the plane and cambered wings. The area enclosed is directly proportional to the drag or thrust developed by the section, depending on whether the area is positive or negative. In traversing the curve starting at the leading edge, moving along the upper surface to the trailing edge and returning along the lower surface to the leading edge, area enclosed on the right results in negative drag or thrust. Likewise, area enclosed on the left results in drag. It is evident from figure 10(a) that at  $M = 0.80$  the cambered wing develops all thrust, whereas the plane wing has some drag associated with the pressures on the lower surface near the leading edge. The thrust developed by the cambered wing is about 1.8 times as large as the thrust developed by the plane wing. In order to assess the effectiveness of the camber, it is convenient to discuss the thrust developed by the section in terms of the theoretical values for full leading-edge suction. The 53-percent-semispan section of the cambered wing develops about 61 percent of full leading-edge suction, whereas the same section of the plane wing develops only about 29 percent. These findings are consistent with the

results noted from reference 2. Figure 10(b) shows the same comparison at  $M = 1.03$ . It is readily apparent that increasing the Mach number from 0.80 to 1.03 was detrimental from a leading-edge thrust standpoint. The thrust developed by the cambered wing is still larger than that developed by the plane wing; however, the magnitude has been reduced considerably. At  $M = 1.03$  this section of the cambered wing developed about 23 percent of full leading-edge suction compared to about 5 percent for the plane wing. Again, the results are consistent with the results of force tests since in figure 8(b) of reference 2 it is shown that the benefits due to camber diminish with increases in Mach number.

Figure 11 presents a comparison of the spanwise load distributions for the plane and cambered wings at several angles of attack and Mach numbers. At  $M = 0.80$  and  $\alpha \approx 4^\circ$ , a decrement in the outboard loadings for the cambered wing is apparent (fig. 11(a)). Such a characteristic would be expected, however, since the camber resulted in the outer portions of the wing operating at a lesser angle of attack than the wing-body center line. With increases in angle of attack to about  $8^\circ$ , the spanwise load distribution for the plane wing deviated markedly from the approximately elliptical shape it had at  $4^\circ$  whereas the shape of the spanwise load distribution for the cambered wing remained the same. Since the cambered wing loading maintains its more nearly elliptical shape to the higher angles of attack, it would be expected to have lower drag due to lift and consequently higher lift-drag ratios at the higher angles. The data of reference 2 bears this out. Examination of the chordwise pressure distributions of references 5 and 10 indicate that the camber delayed the separation over the outboard sections of the wing to a higher angle of attack. The delayed separation, in turn, is responsible for the differences in the shapes of the spanwise load distributions at  $\alpha \approx 8^\circ$ . At an angle of attack of about  $12^\circ$ , both the plane and cambered wings appear to be separated over the outboard regions. At  $M = 1.03$  (fig. 11(b)) the same trends are apparent; however, the separation characteristics for the plane wing do not appear to be as marked as they were at  $M = 0.80$ .

## CONCLUSIONS

An investigation to determine the aerodynamic loading characteristics of a thin conical cambered low-aspect-ratio delta wing in combination with basic and indented bodies has been conducted in the Langley 8-foot transonic tunnels at Mach numbers from 0.60 to 1.43. The data have been analyzed and indicate the following conclusions:

1. At subsonic speeds and at moderate angles of attack, a leading-edge separation vortex causes the span load distributions to deviate from their approximately elliptical shape and approach triangular at the

highest angle tested. The effect of this vortex is not so prominent at the higher test Mach numbers.

2. Rearward and outboard center-of-pressure movements, of the order of 9 percent of the mean aerodynamic chord and 2 percent of the semispan, respectively, occurred between Mach numbers of 0.85 and 1.0. Also, some forward and inboard movements are noted at subsonic speeds at high normal-force coefficients.

3. The effects of body indentation on the aerodynamic loading characteristics are small.

4. Comparisons with experimental data for a similar plane wing indicate that the cambered wing is much more effective in utilizing the wing leading-edge suction pressure to develop leading-edge thrust at subsonic speeds. With increases in Mach number, the benefit due to camber diminishes.

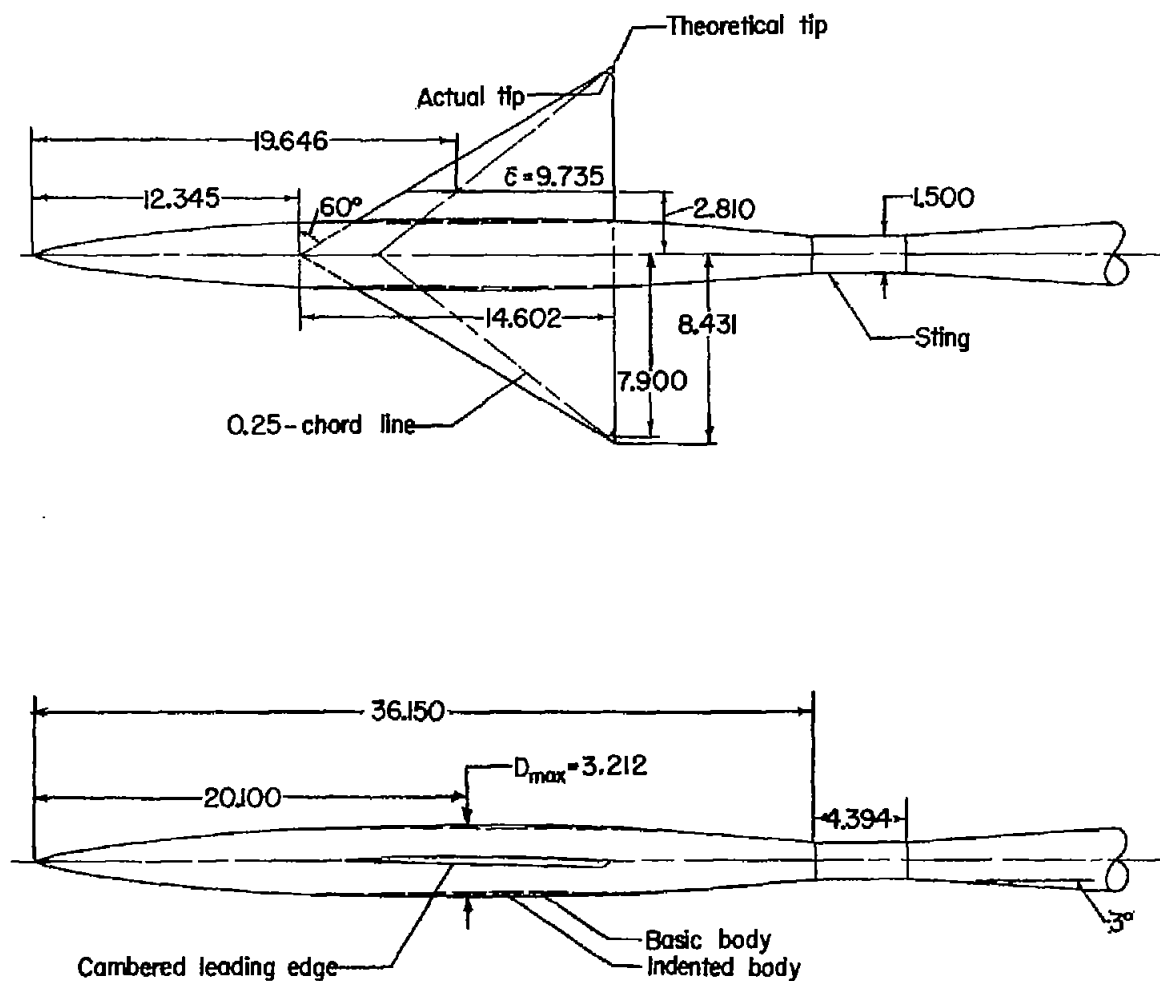
Langley Aeronautical Laboratory,  
National Advisory Committee for Aeronautics,  
Langley Field, Va., June 11, 1958.

~~CONFIDENTIAL~~

## REFERENCES

1. Saltzman, Edwin J., Bellman, Donald R., and Musialowski, Norman T.: Flight-Determined Transonic Lift and Drag Characteristics of the YF-102 Airplane With Two Wing Configurations. NACA RM H56E08, 1956.
2. Mugler, John P., Jr.: Effects of Two Leading-Edge Modifications on the Aerodynamic Characteristics of a Thin Low-Aspect-Ratio Delta Wing at Transonic Speeds. NACA RM L56G12a, 1956.
3. Kelly, Thomas C.: Transonic Wind-Tunnel Investigation of Aerodynamic-Loading Characteristics of a 2-Percent-Thick Trapezoidal Wing in Combination With Basic and Indented Bodies. NACA RM L56J12a, 1957.
4. Fischetti, Thomas L.: Investigation at Mach Numbers From 0.80 to 1.43 of Pressure and Load Distributions Over a Thin  $45^\circ$  Sweptback Highly Tapered Wing in Combination With Basic and Indented Bodies. NACA RM L57D29a, 1957.
5. Mugler, John P., Jr.: Pressure Measurements at Transonic and Low Supersonic Speeds on a Thin Conical Cambered Low-Aspect-Ratio Delta Wing in Combination With Basic and Indented Bodies. NACA RM L57G19, 1957.
6. Ritchie, Virgil S., and Pearson, Albin O.: Calibration of the Slotted Test Section of the Langley 8-Foot Transonic Tunnel and Preliminary Experimental Investigation of Boundary-Reflected Disturbances. NACA RM L51K14, 1952.
7. Mathews, Clarence W.: An Investigation of the Adaptation of a Transonic Slotted Tunnel to Supersonic Operation by Enclosing the Slots With Fairings. NACA RM L55H15, 1955.
8. Burnett, H. R.: Geometry of Cambered Leading Edges and Warped Tips To Be Evaluated in the NACA 8-Ft. and  $4 \times 4$  Ft. Tunnels for the F-102 Airplane. Aero Memo A-8-44 (Contract No. AF33(600)-5942), Consolidated Vultee Aircraft Corp., May 27, 1953.
9. Whitcomb, Richard T., and Fischetti, Thomas L.: Development of a Supersonic Area Rule and an Application to the Design of a Wing-Body Combination Having High Lift-to-Drag Ratios. NACA RM L53H31a, 1953.
10. Swihart, John M., and Foss, Willard E., Jr.: Transonic Loads Characteristics of a 3-Percent-Thick  $60^\circ$  Delta-Wing-Body Combination. NACA RM L57D12, 1957.

~~CONFIDENTIAL~~

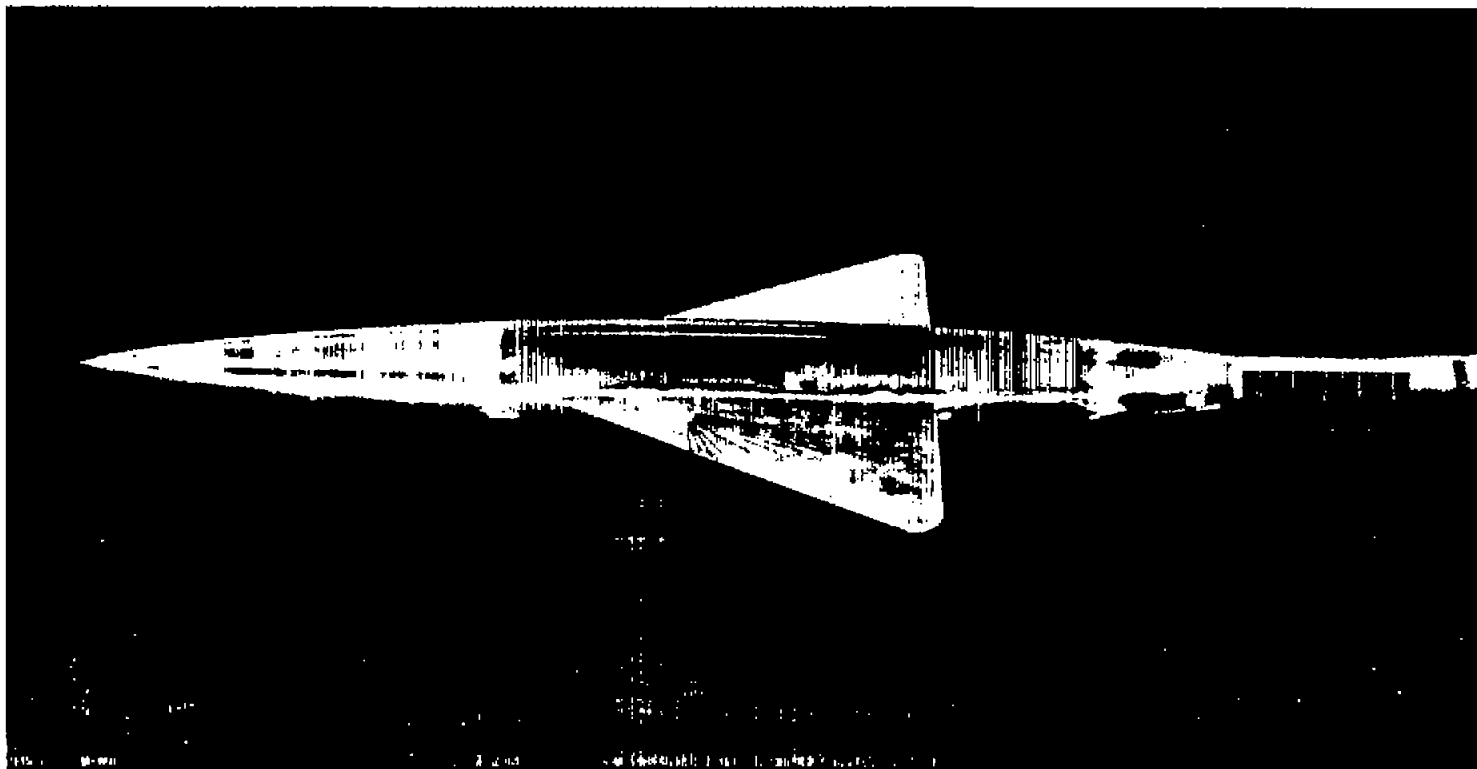


(a) Wing-body combinations.

Figure 1.- Model details. All dimensions are in inches unless otherwise noted.

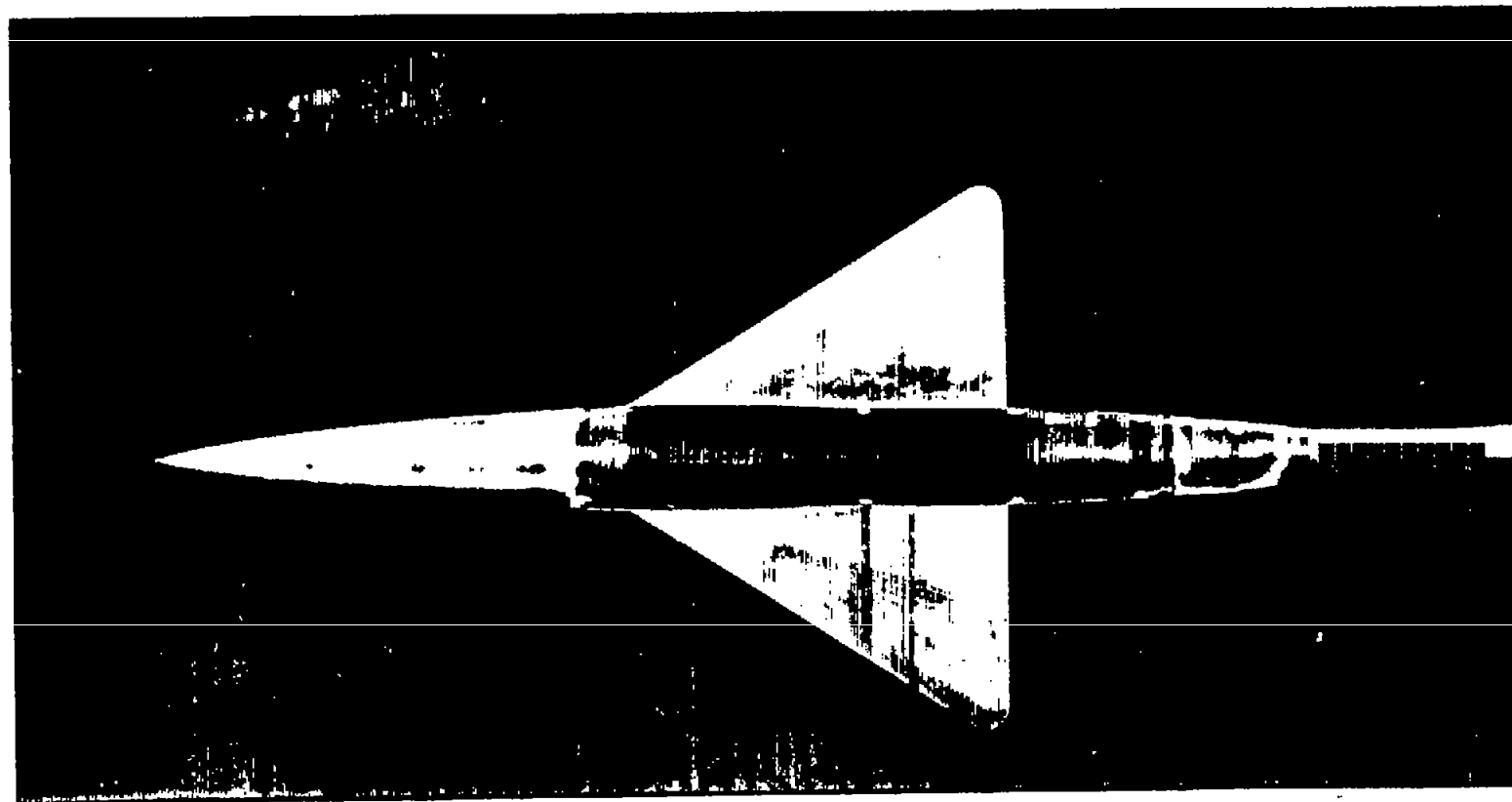






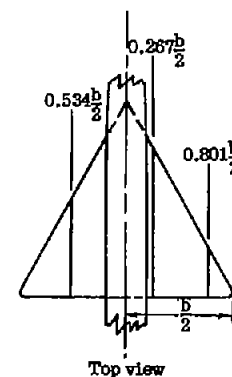
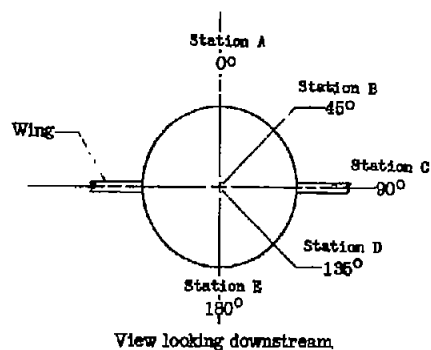
(c) Photograph of basic wing-body combination. L-89613

Figure 1.- Continued.



(d) Photograph of indented wing-body combination. L-89620

Figure 1.- Concluded.



Location of body pressure orifices, $\frac{x}{l}$				
Meridian, 0, deg	Meridian, 45, deg	Meridian, 90, deg	Meridian, 135, deg	Meridian, 180, deg
0.055	0.168	0.055	0.166	0.055
.168	.277	.168	.277	.168
.277	.387	.277	.387	.277
.387	.387	.383	.387	.387
.387	.443	.387	.443	.387
.415	.498	.747*	.498	.443
.443	.553	.775	.553	.498
.498	.609	.830	.609	.553
.553	.664	.871	.664	.609
.581	.719	.954	.719	.664
.609	.775		.775	.719
.638	.830		.830	.775
.664	.871		.871	.830
.692				.871
.719				.954
.747				
.775				
.830				
.871				
.954				

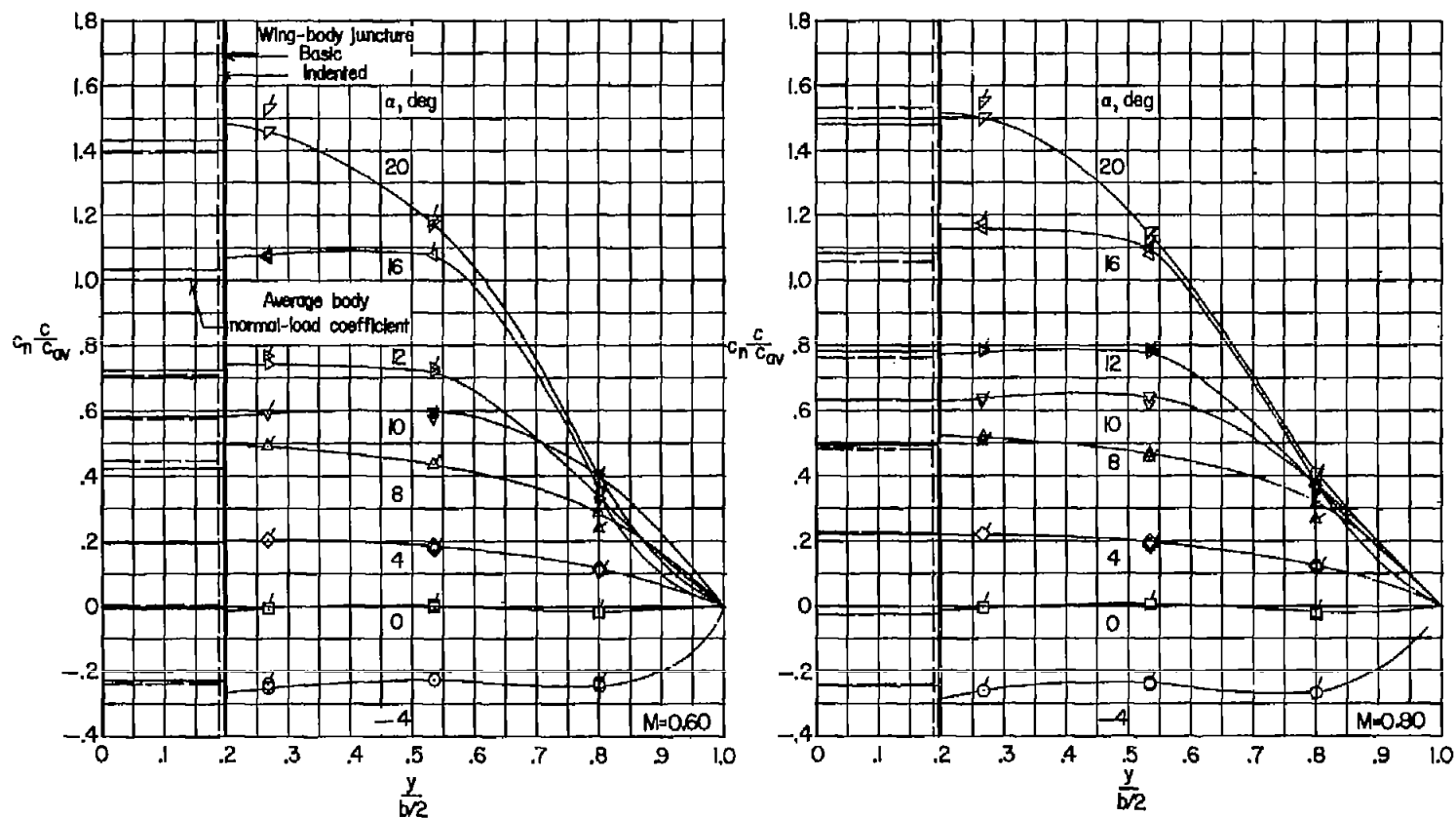
\*Indented body only

Location of wing pressure orifices, $\frac{x}{a}$					
0.287 $\frac{b}{2}$		0.534 $\frac{b}{2}$		0.801 $\frac{b}{2}$	
Upper surface	Lower surface	Upper surface	Lower surface	Upper surface	Lower surface
0.010	0.025	0.010	0.025	0.030	0.045
.030	.060	.030	.060	.060	.150
.060	.100	.060	.100	.100	.250
.100	.150	.100	.200	.200	.350
.150	.200	.200	.300	.300	.450
.200	.300	.300	.400	.400	.550
.300	.400	.400	.500	.500	.650
.400	.500	.500	.600	.600	.750
.500	.600	.600	.700	.700	
.600	.700	.700	.800	.850	
.700	.800	.800	.850		
.800	.850	.900			
.900	.925				
.950					

(a) On basic and indented body.

(b) On wing.

Figure 2.- Location of pressure orifices.



(a)  $M = 0.60$  and  $0.80$ .

Figure 3.- Spanwise load distributions. Flagged symbols and dashed lines indicated indented body data.

~~CONFIDENTIAL~~

NACA RM 158724

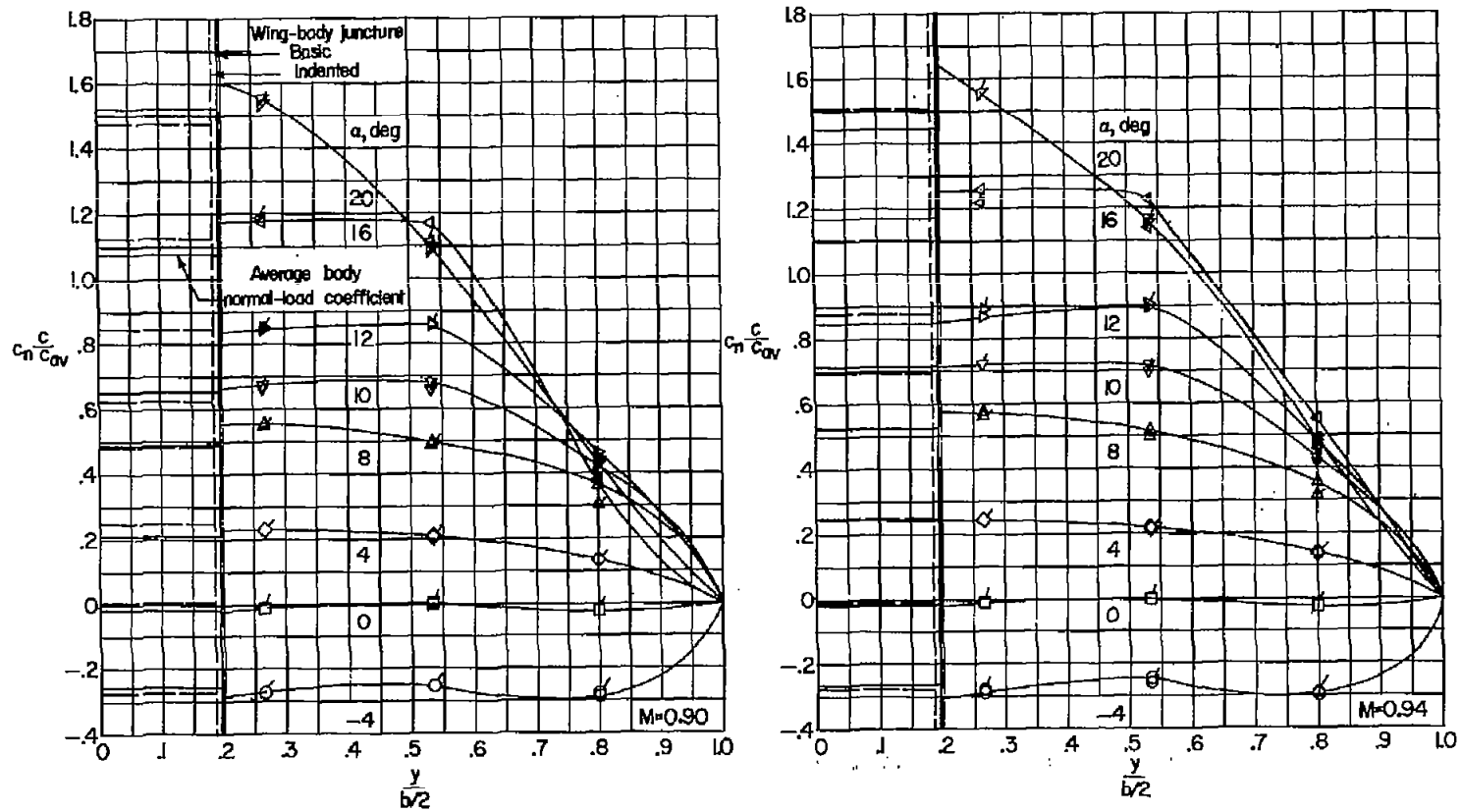
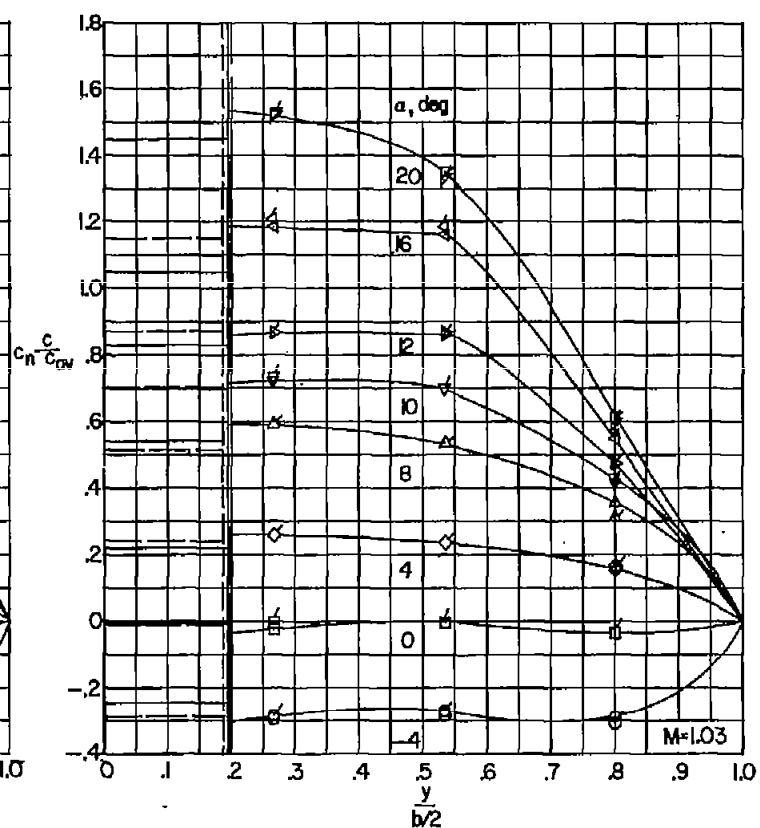
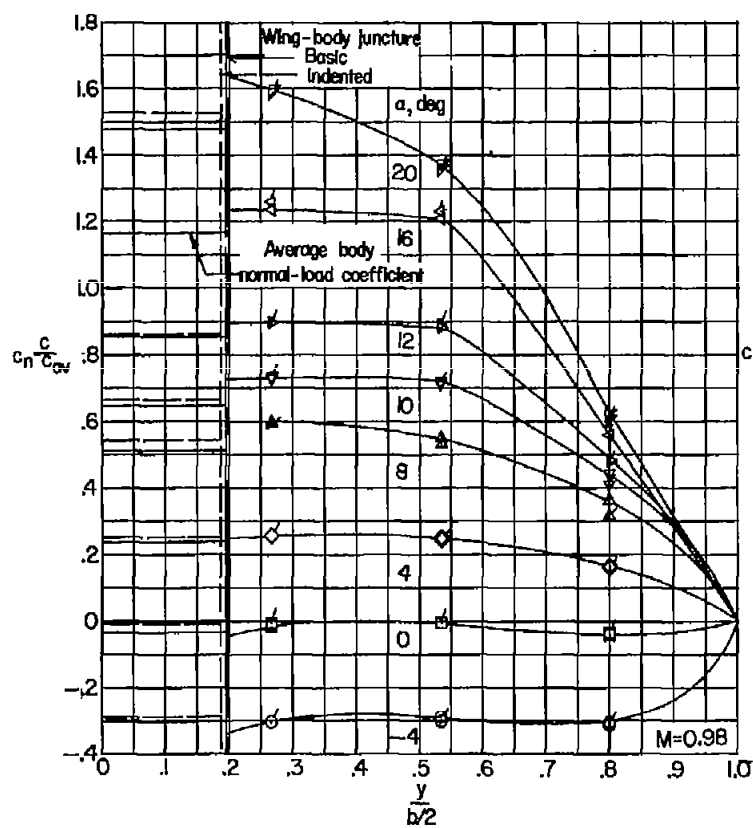
(b)  $M = 0.90$  and  $0.94$ .

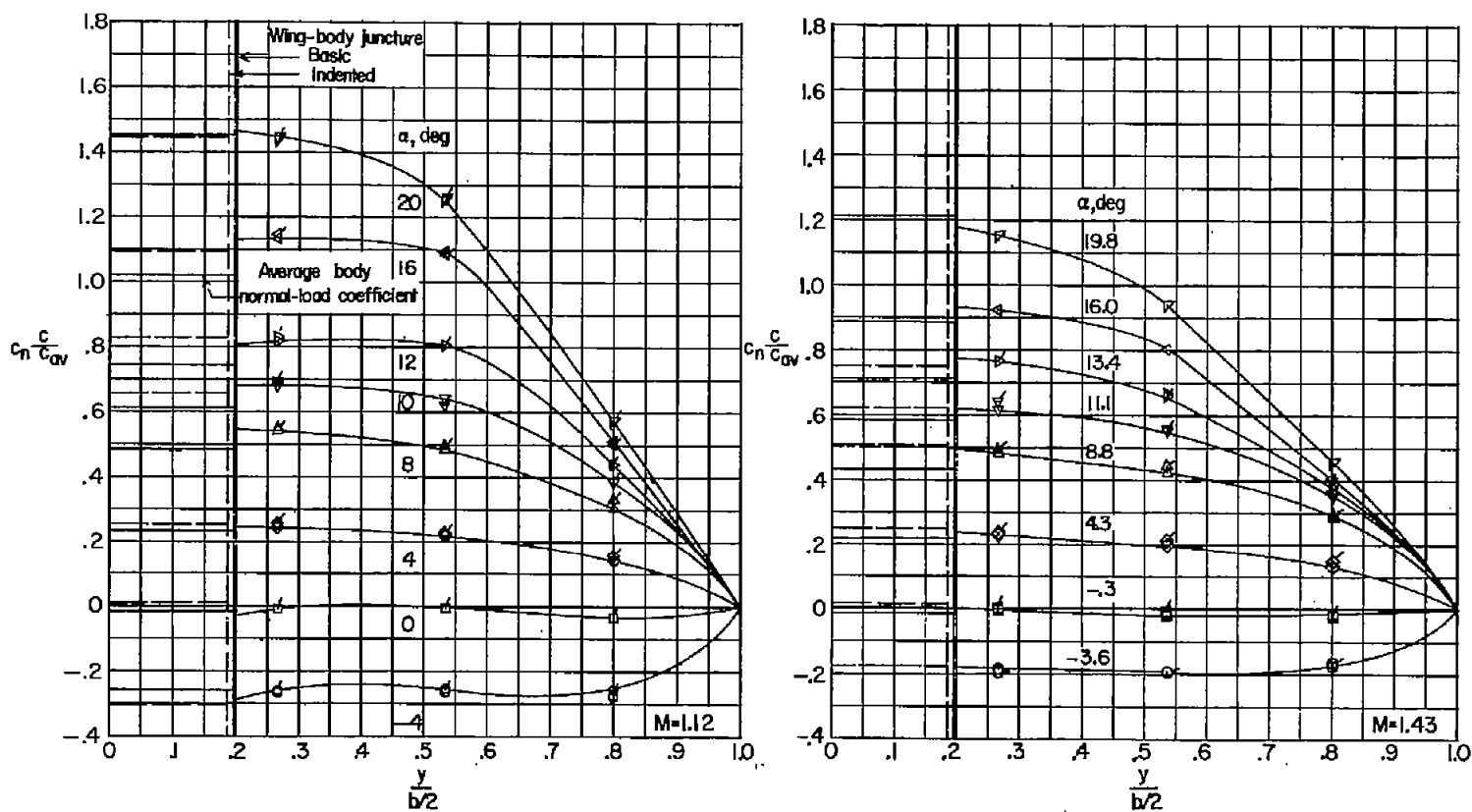
Figure 3.- Continued.

~~CONFIDENTIAL~~



(c)  $M = 0.98$  and  $1.03$ .

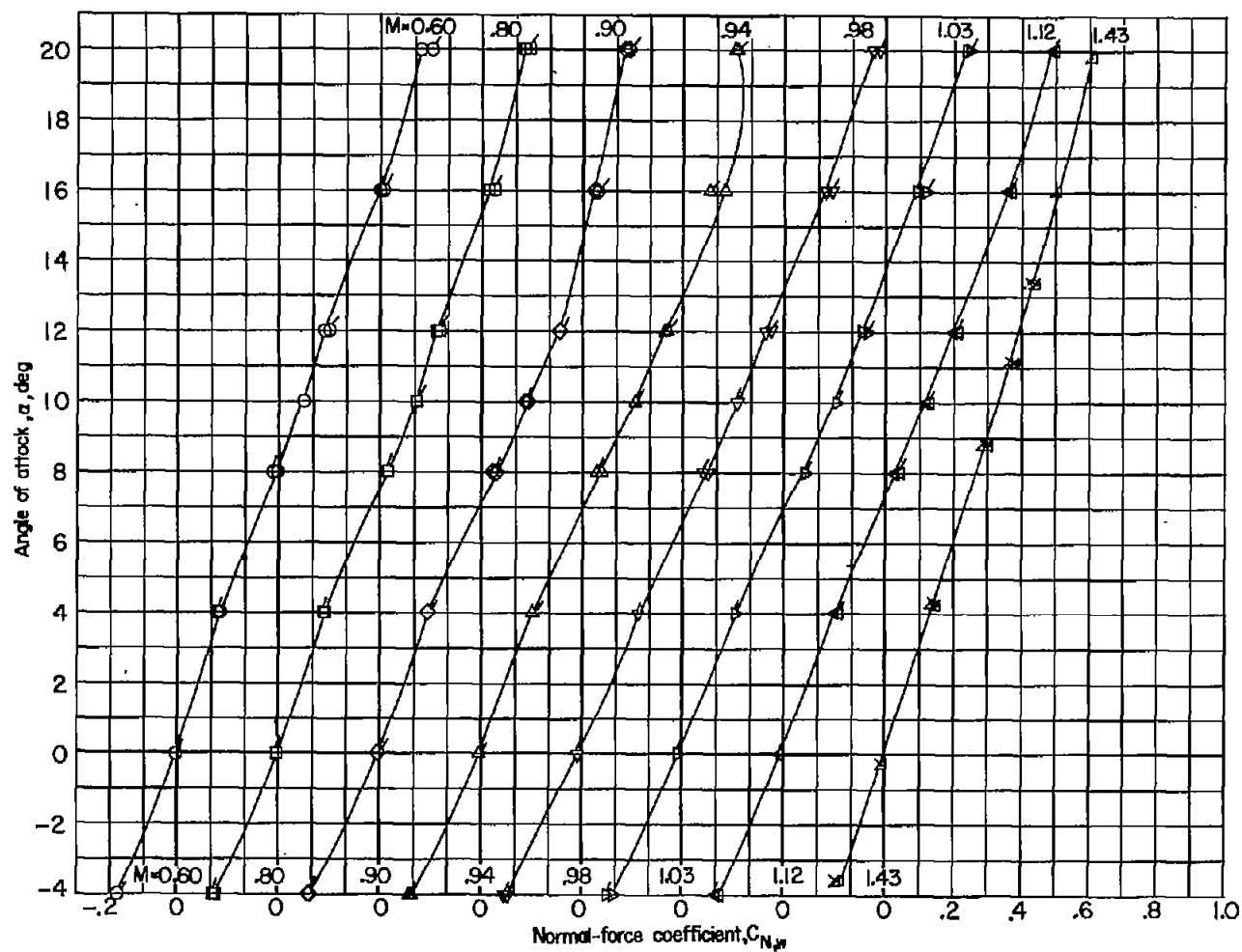
Figure 3.- Continued.



(d)  $M = 1.12$  and  $1.43$ .

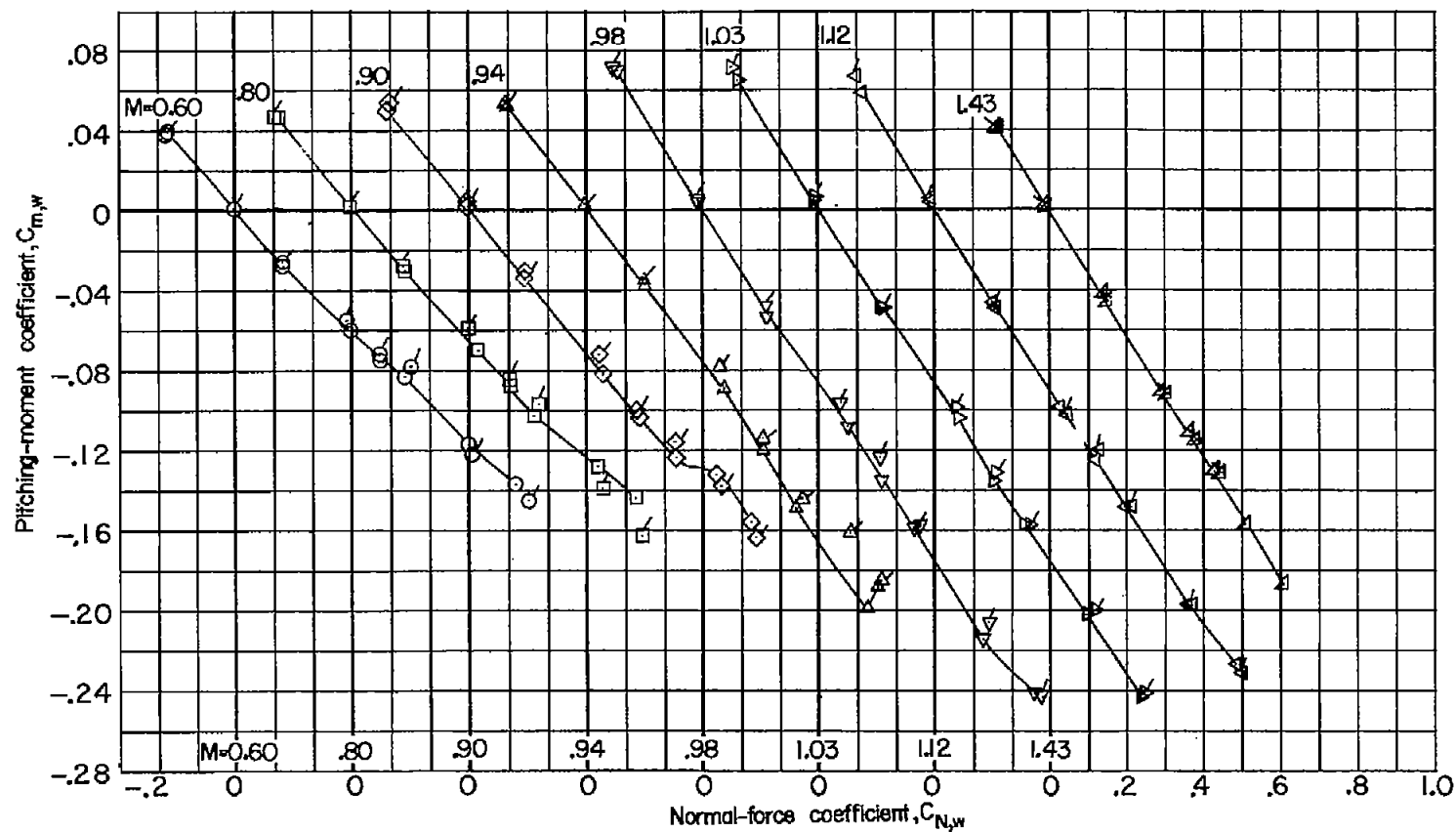
Figure 3.- Concluded.





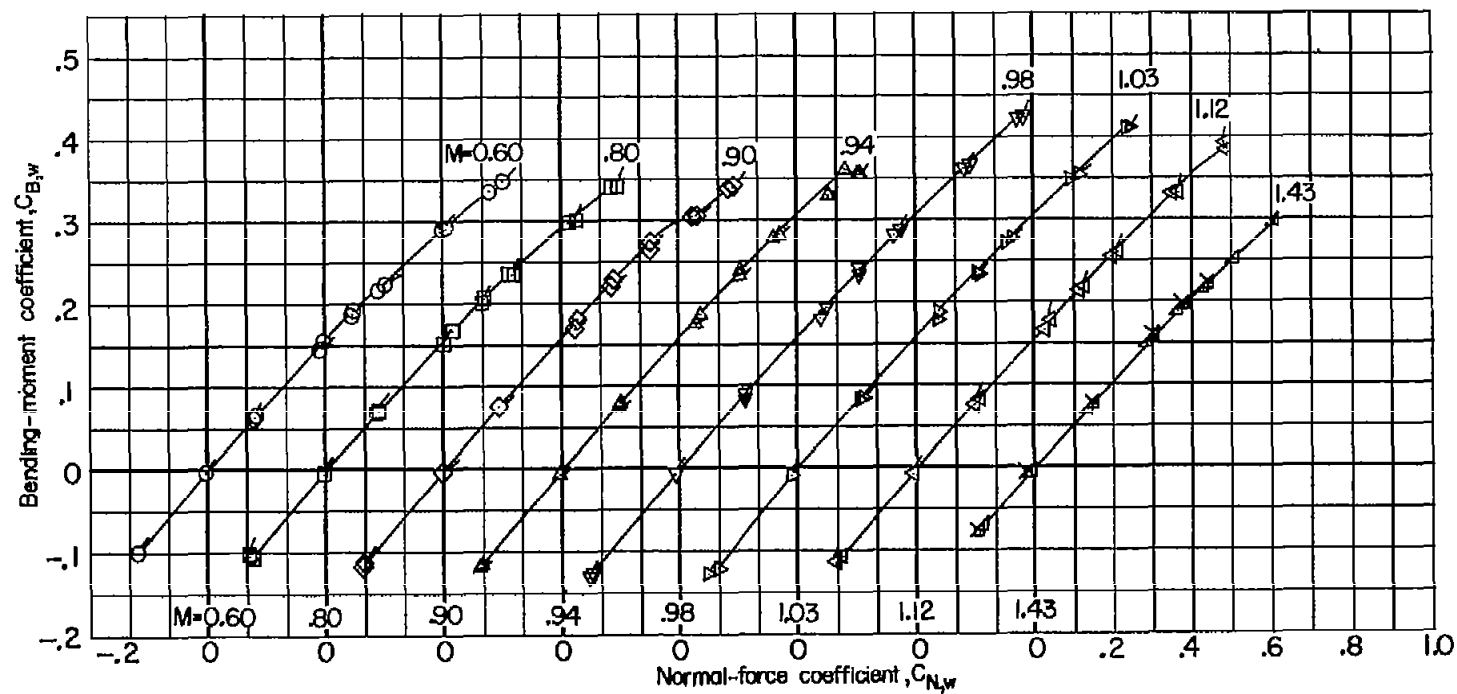
(a)  $\alpha$  plotted against  $C_{N,w}$ .

Figure 4.- Aerodynamic characteristics of the wing in the presence of the body. Flagged symbols denote data for the indented body.



(b)  $C_{m,w}$  plotted against  $C_{N,w}$ .

Figure 4.- Continued.



(c)  $C_{B,w}$  plotted against  $C_{N,w}$ .

Figure 4.- Concluded.

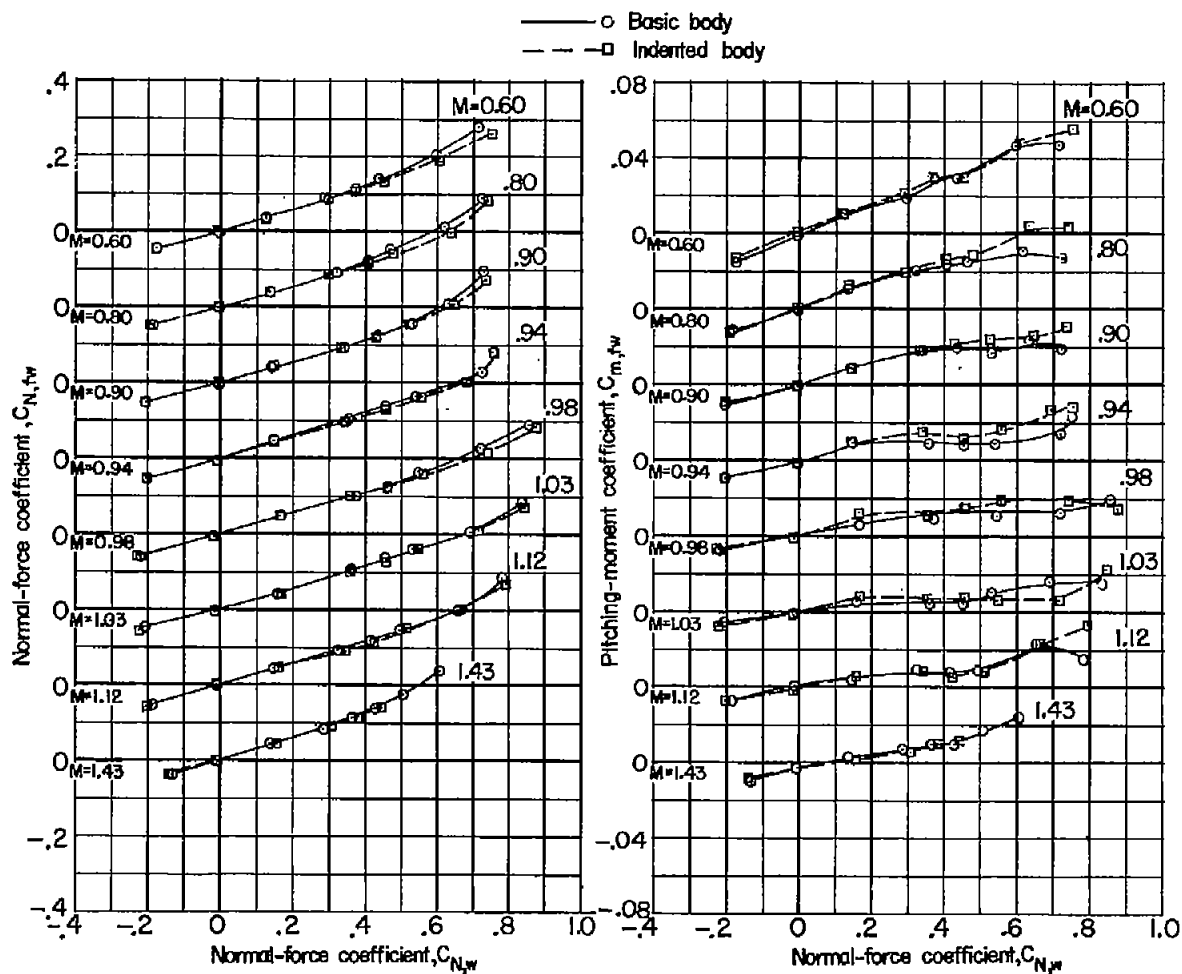
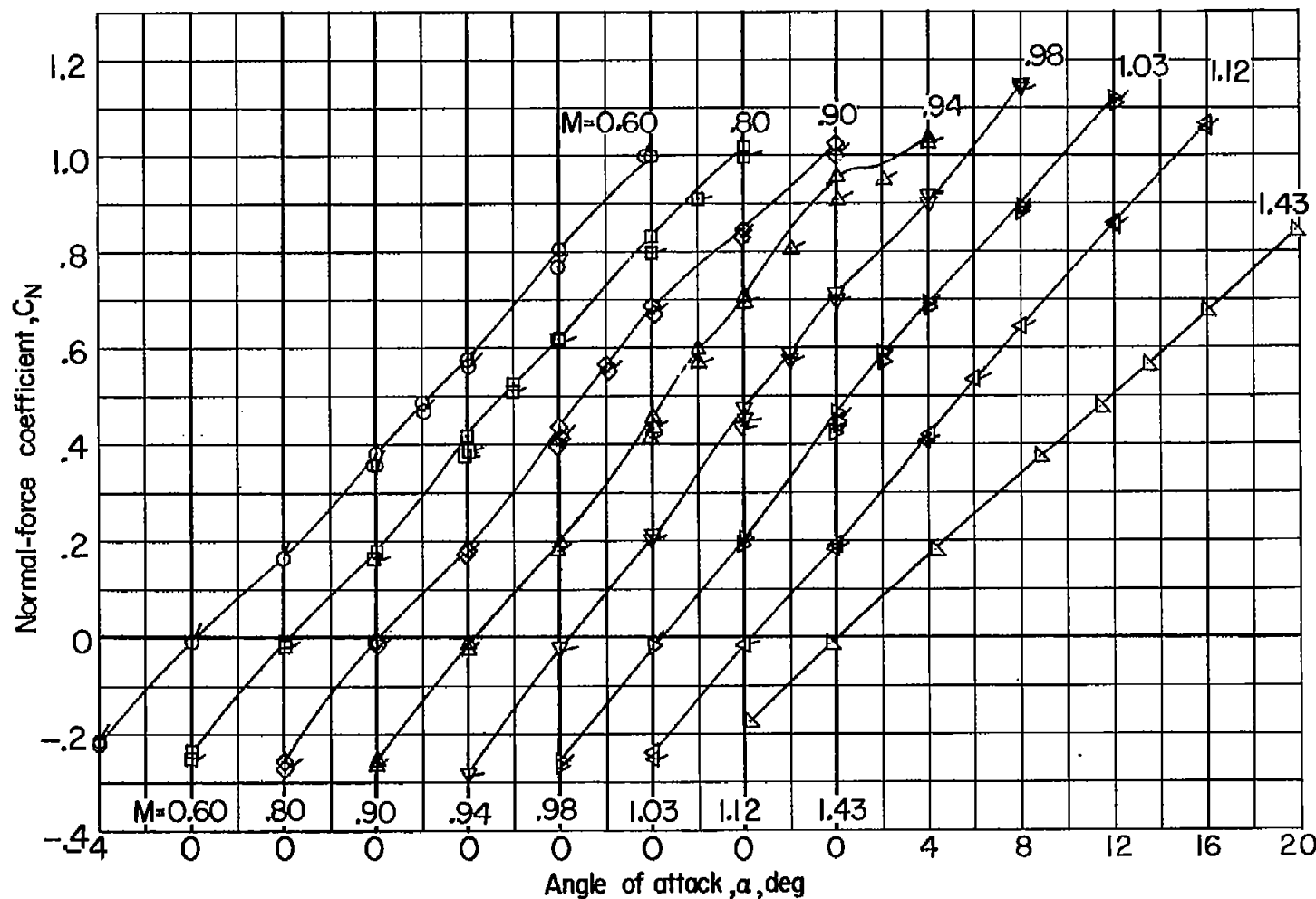
(a)  $C_{N,fw}$  plotted against  $C_{N,w}$ .(b)  $C_{m,fw}$  plotted against  $C_{N,w}$ .

Figure 5.- Aerodynamic characteristics of the basic and indented bodies in the presence of the wing.



(a)  $C_N$  plotted against  $\alpha$ .

Figure 6.- Aerodynamic characteristics of the basic wing-body combination. Flagged symbols denote force data for same configuration from reference 2.

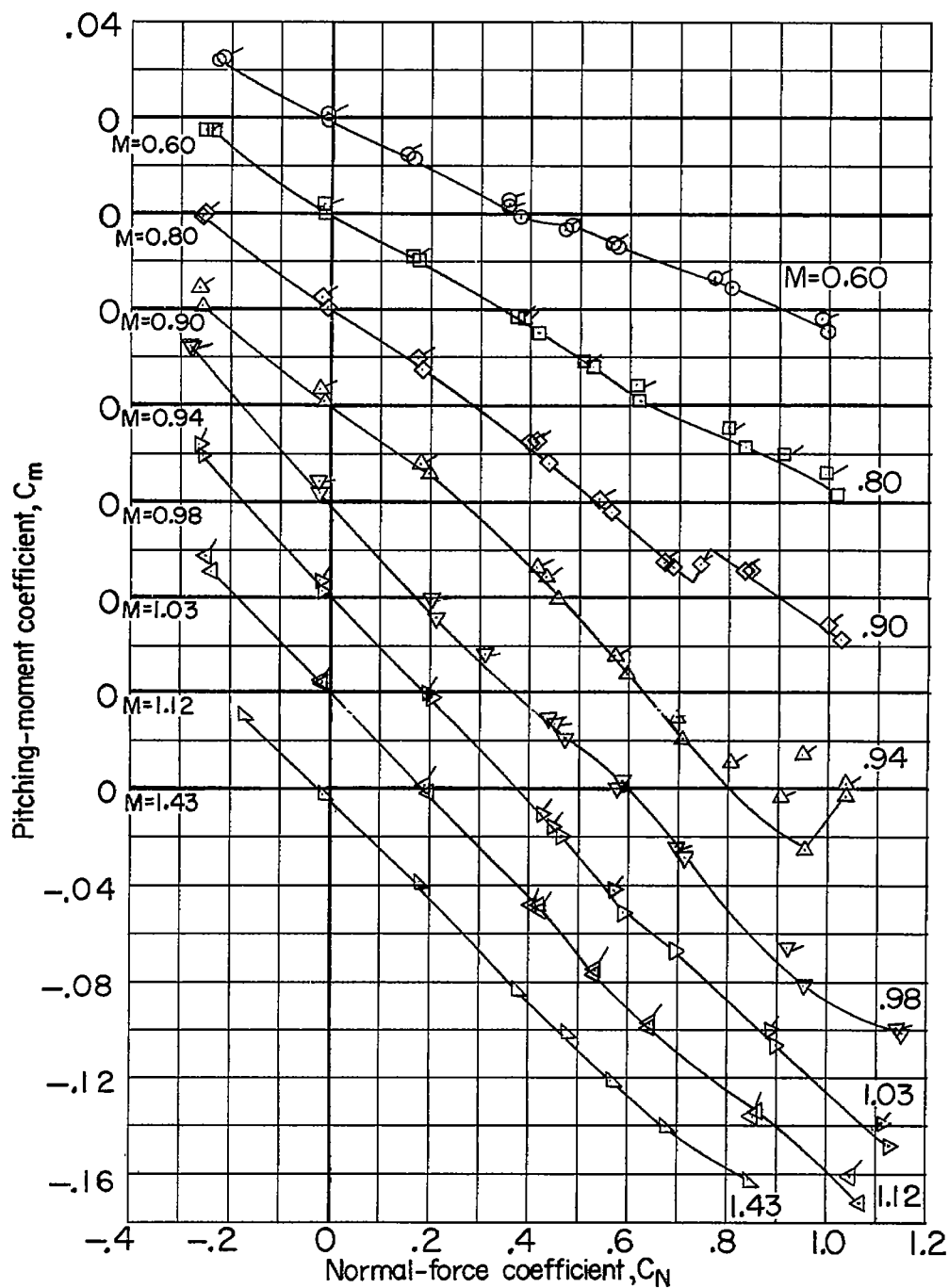
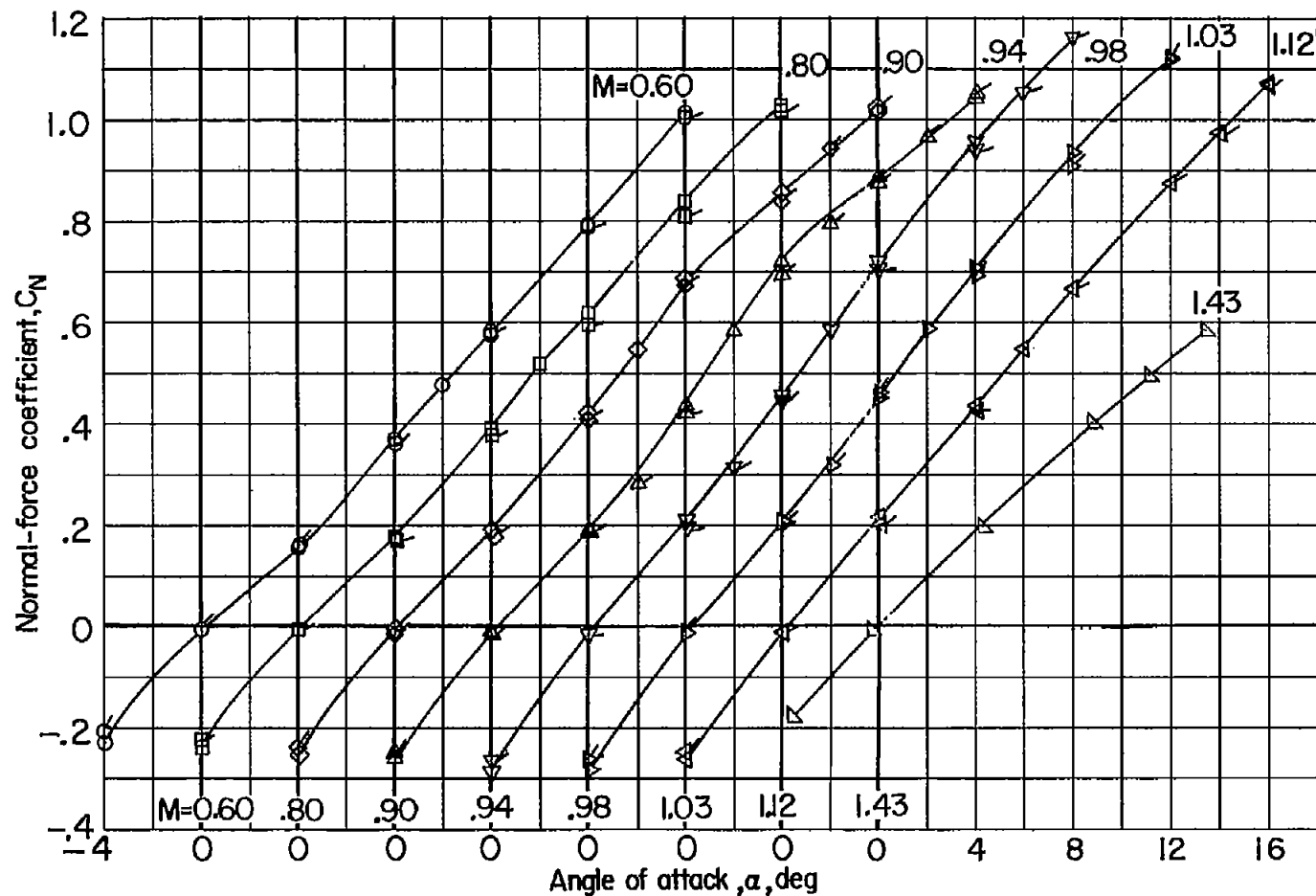
(b)  $C_m$  plotted against  $C_N$ .

Figure 6.- Concluded.



(a)  $C_N$  plotted against  $\alpha$ .

Figure 7.- Aerodynamic characteristics of the indented wing-body combination. Flagged symbols denote force data for same configuration from reference 2.

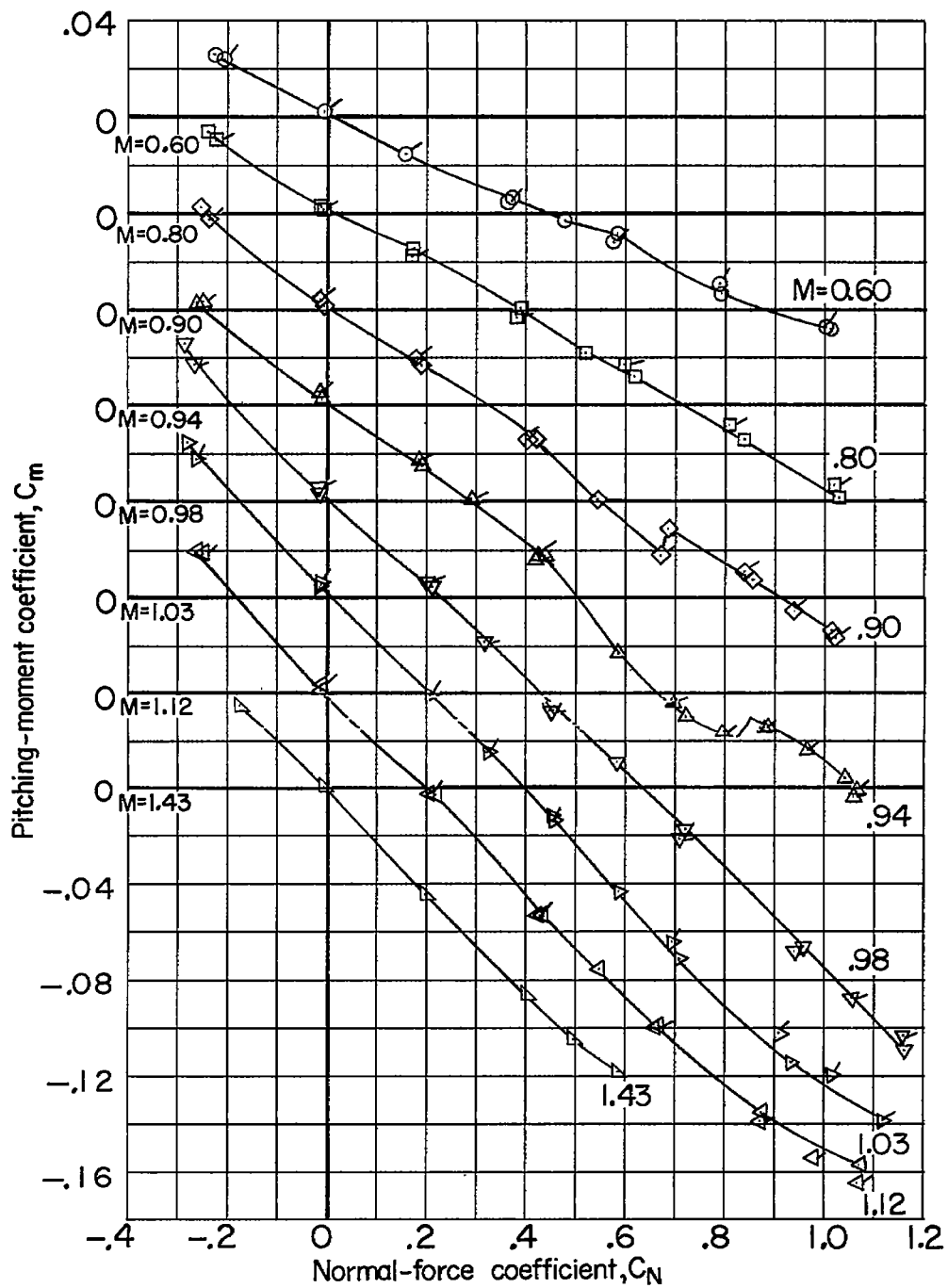
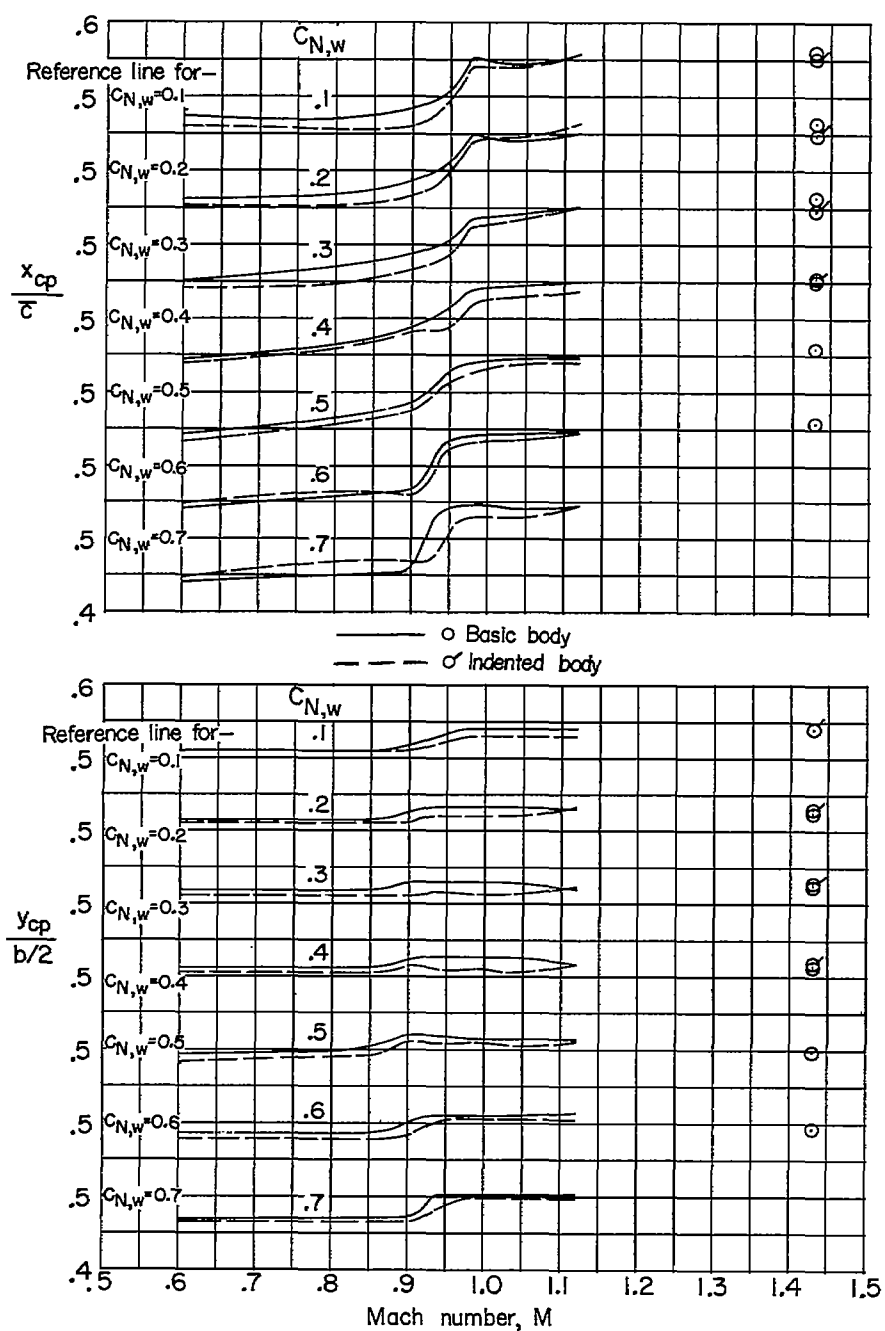
(b)  $C_m$  plotted against  $C_N$ .

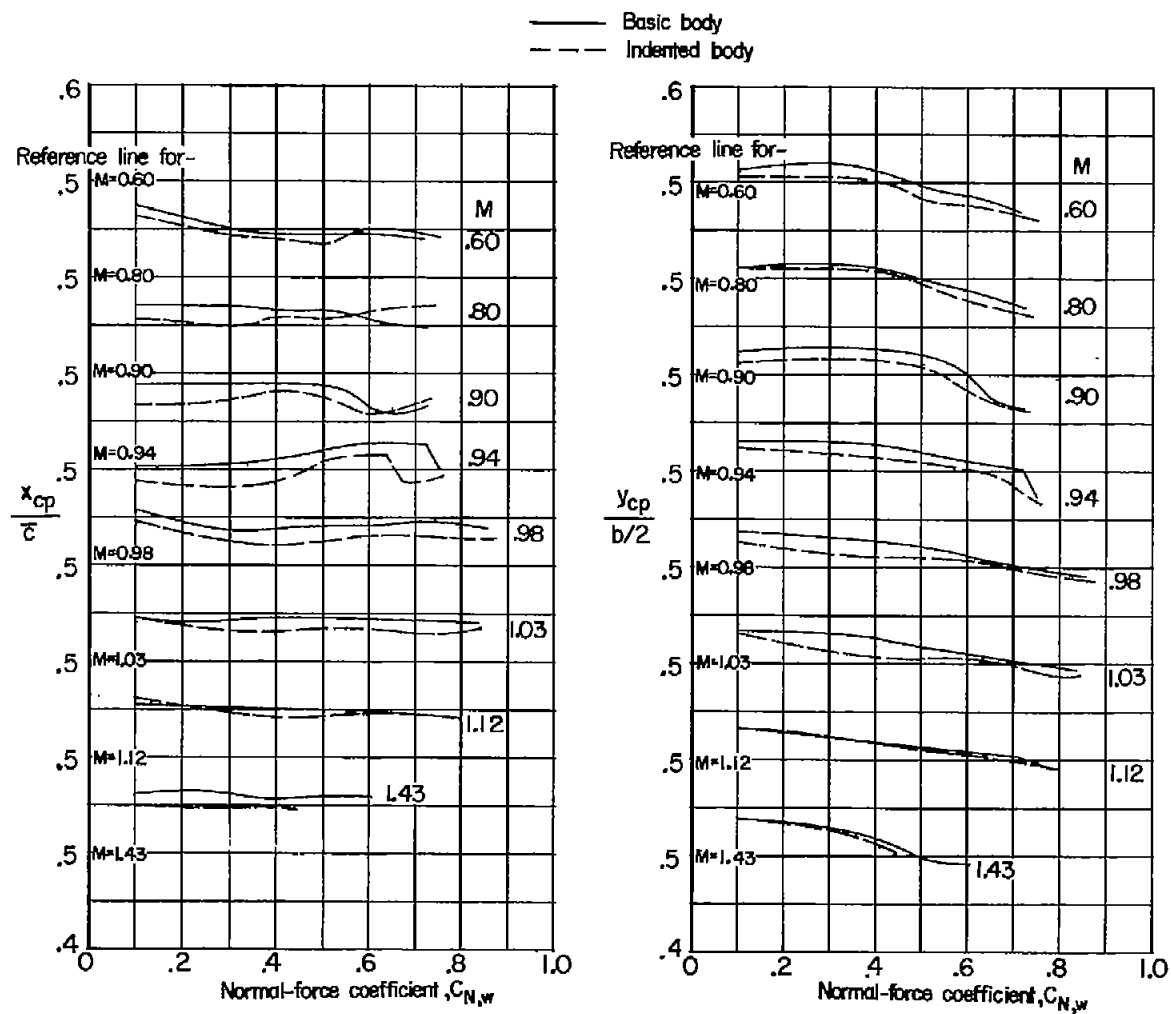
Figure 7.- Concluded.





(a) Variation with Mach number.

Figure 8.- Variation of longitudinal and lateral location of center of pressure.



(b) Variation with wing normal-force coefficient.

Figure 8.- Concluded.

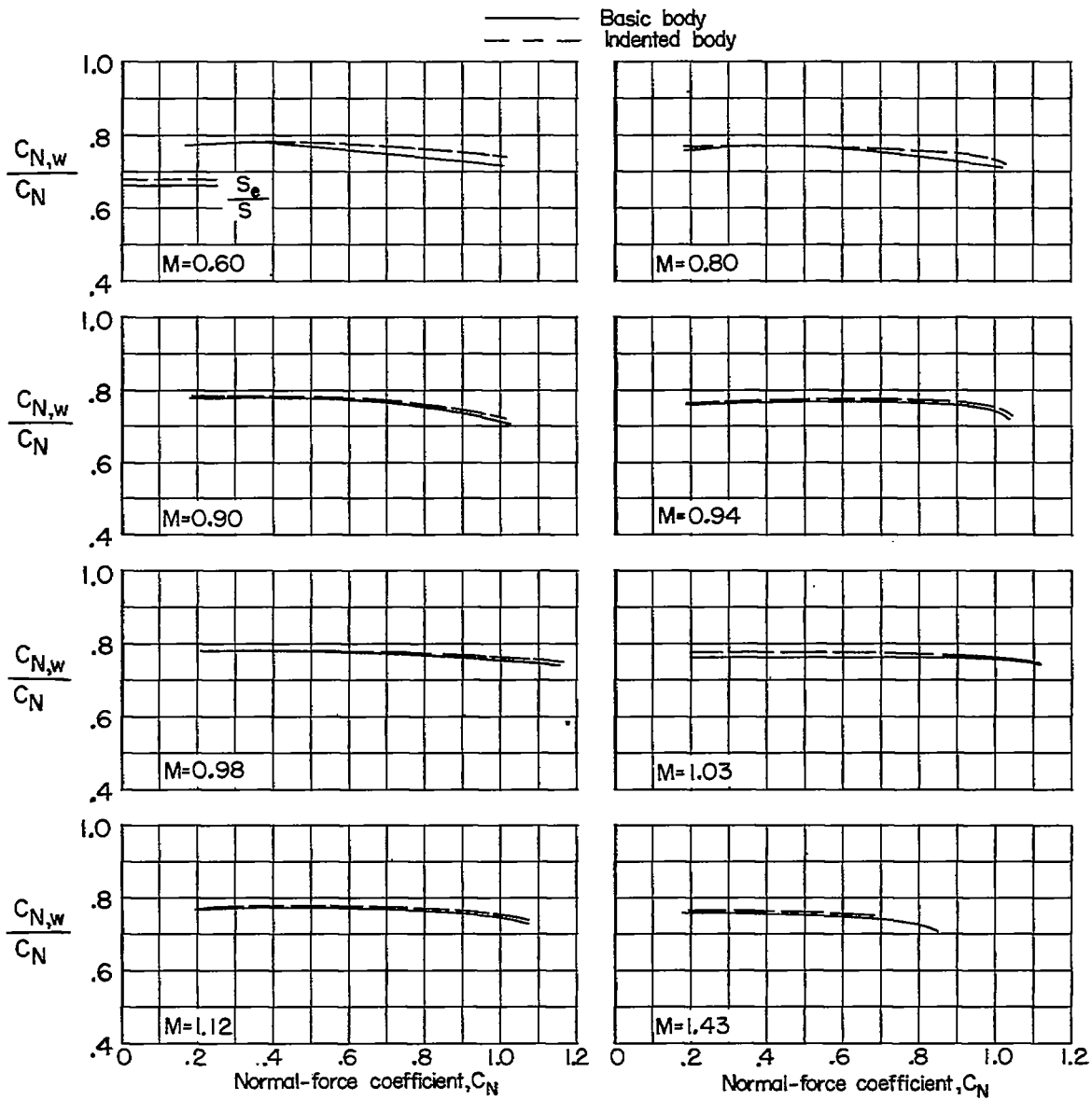
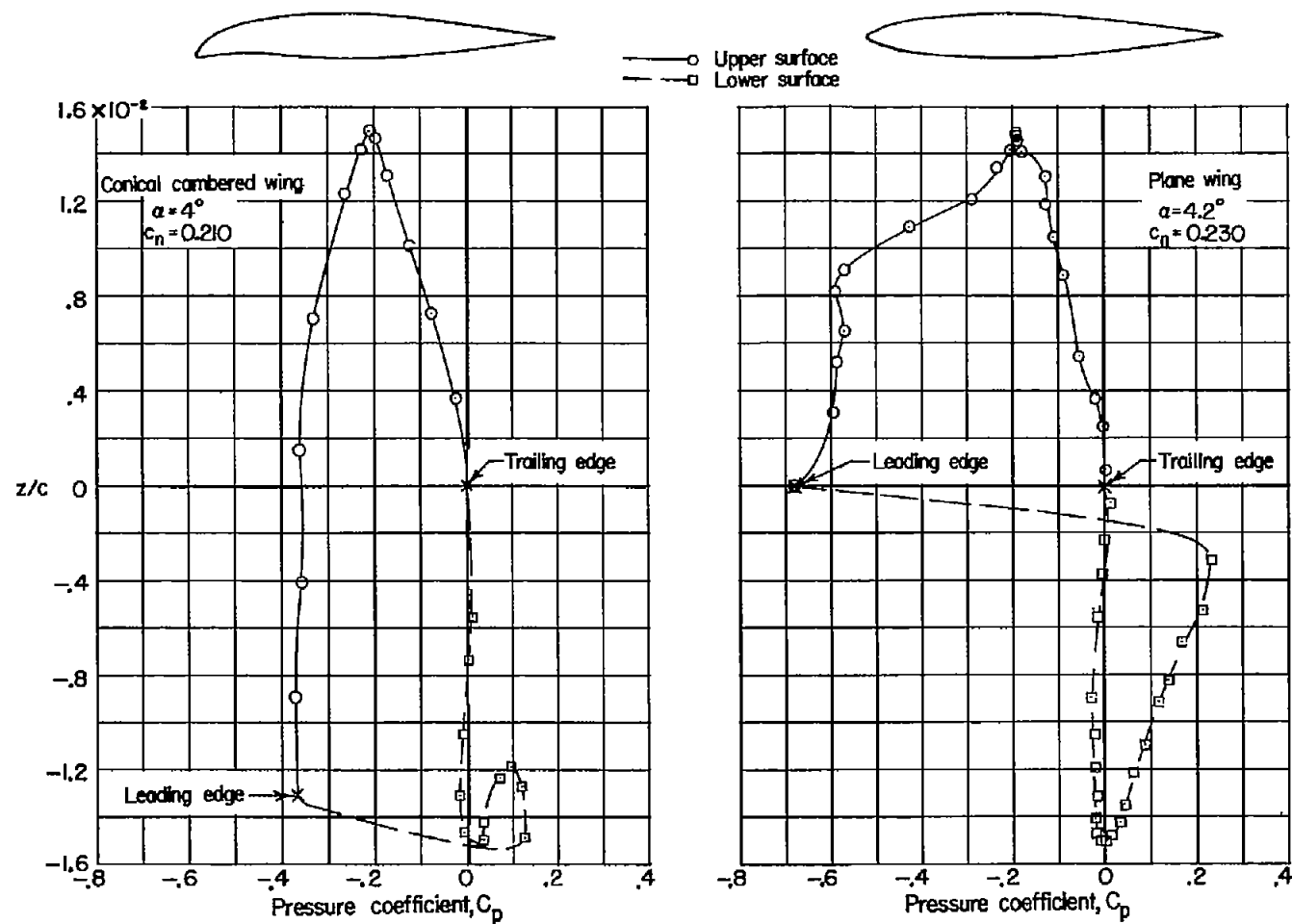


Figure 9.- Division of normal load.



(a)  $M = 0.80$ .

Figure 10.- Comparison of pressure distributions for the plane and cambered wings. Data for plane wing from reference 10.

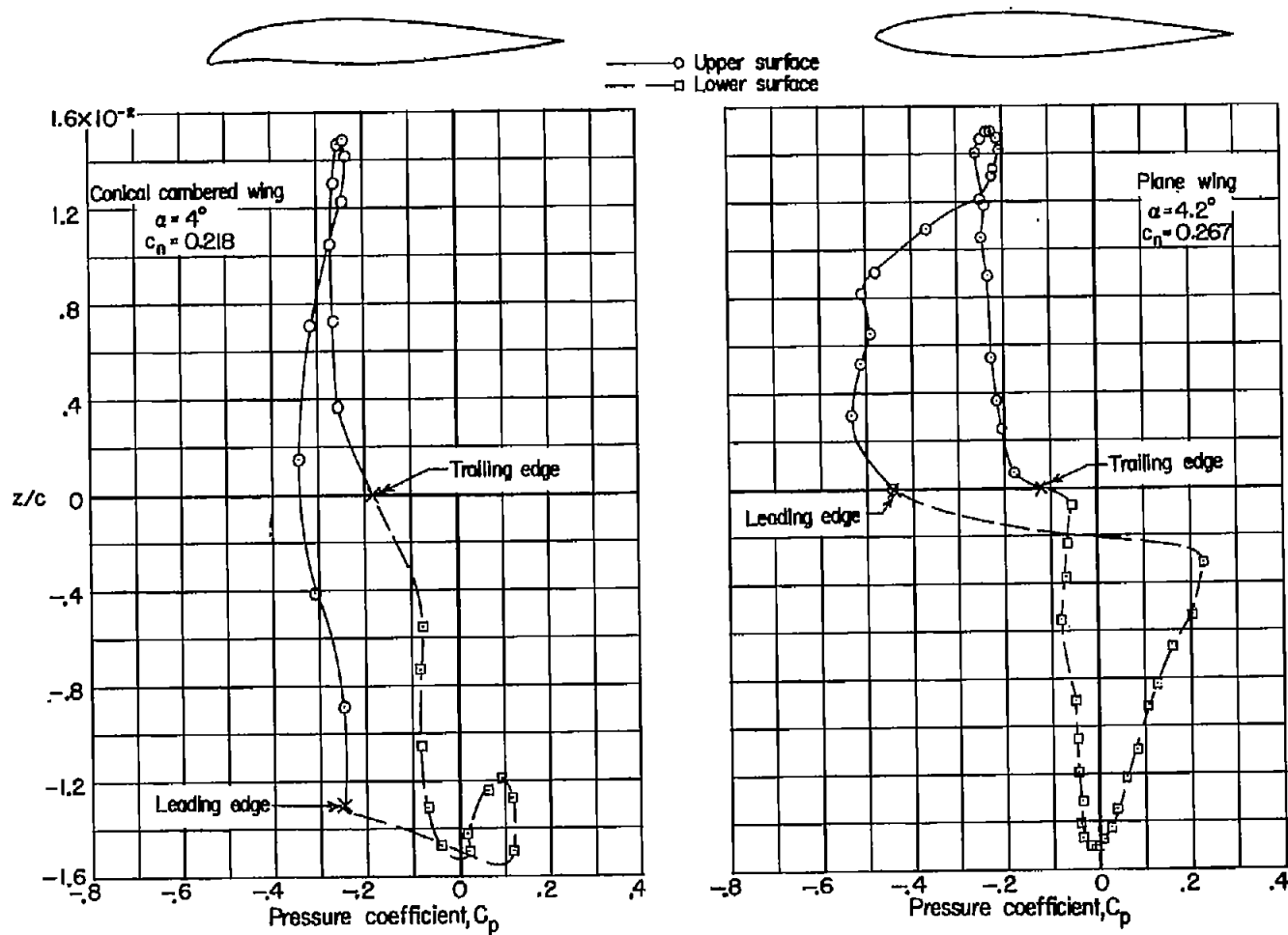
(b)  $M = 1.03$ .

Figure 10.- Concluded.

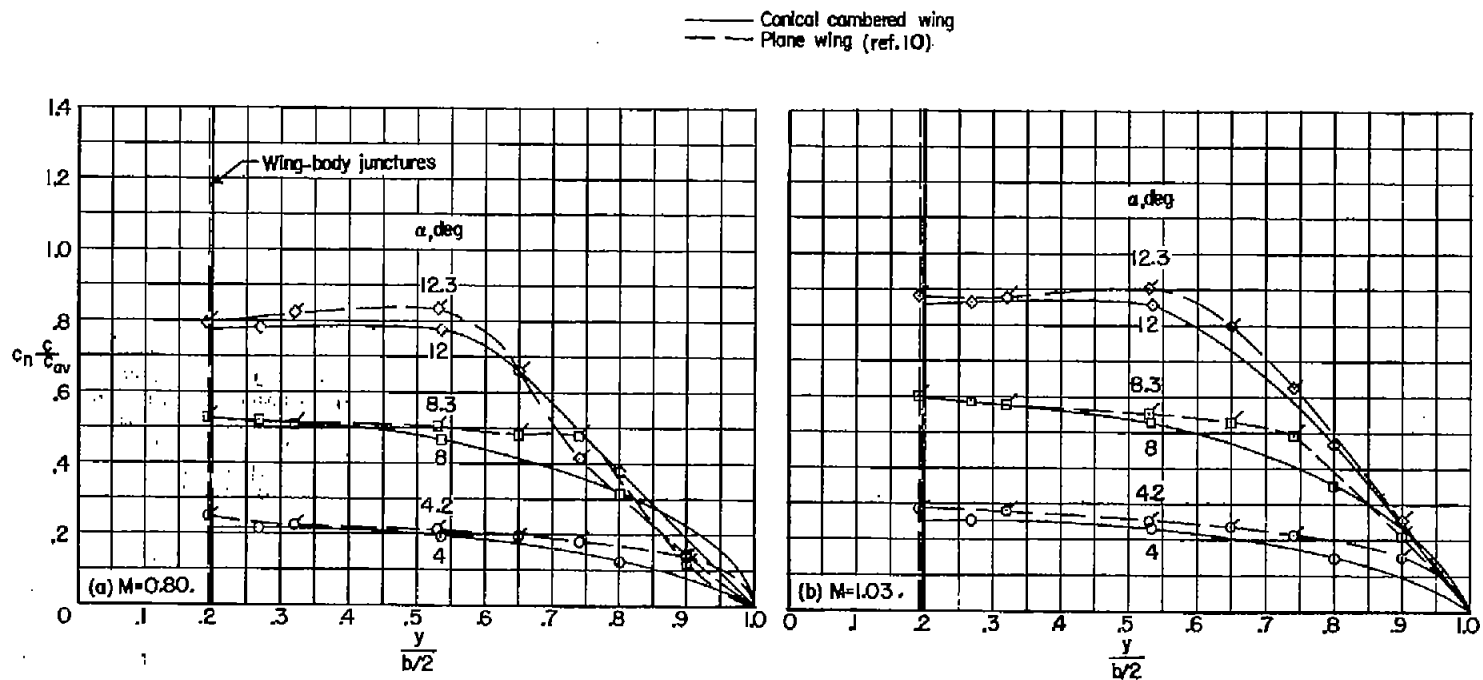


Figure 11.- Comparison of span loading characteristics for the plane and cambered wings.